

Article

Spectroscopic and Morphologic Investigation of Bronze Disease: Performance Evaluation of Portable Devices

Daniela Porcu ^{1,2,*} , Silvia Innocenti ² , Monica Galeotti ³, Jana Striova ², Luigi Dei ¹, Emiliano Carretti ¹ 
and Raffaella Fontana ²

¹ Department of Chemistry “Ugo Schiff” and CSGI Consortium, University of Florence, Via della Lastruccia 3-13, 50019 Sesto Fiorentino, FI, Italy

² National Research Council—National Institute of Optics (CNR-INO), Largo E. Fermi 6, 50125 Florence, FI, Italy

³ Opificio Delle Pietre Dure, Via Degli Alfani 78, 50121 Florence, FI, Italy

* Correspondence: daniela.porcu@unifi.it

Abstract: Copper alloy artworks are particularly subjected to chloride attack, which may trigger bronze disease. Therefore, early identification of the phenomenon is crucial in order to stabilize the reactive copper chloride (CuCl) and remove the harmful corrosion products (atacamite and polymorphs). Confocal Raman Microspectroscopy (CRM) has proven to be effective for the detection of small amounts of atacamite, ascribable to the initial phases of corrosion. The handling of bronze artworks is often difficult or even impossible given their large size and weight, and sampling is not always allowed, making the use of portable instruments mandatory for on-site diagnostics. This paper proposes a method for the early detection of corrosion using non-invasive approaches. In this work, we present the results obtained from a set of artificially aged bronze samples with a suite of either laboratory (bench-top) or field (portable/transportable) instruments with the aim of highlighting their characteristics and performances in the diagnosis of bronze disease. Raman spectroscopy, Fiber Optics Reflectance Spectroscopy (FORS), Optical Coherence Tomography (OCT), and Scanning Electron Microscopy (SEM) were applied for chemical and morphological characterization of the samples.

Keywords: copper trihydroxychlorides; bronze disease; artificial patina formation; cultural heritage; OCT; Raman spectroscopy; FORS; SEM



Citation: Porcu, D.; Innocenti, S.; Galeotti, M.; Striova, J.; Dei, L.; Carretti, E.; Fontana, R. Spectroscopic and Morphologic Investigation of Bronze Disease: Performance Evaluation of Portable Devices. *Heritage* **2022**, *5*, 3548–3561. <https://doi.org/10.3390/heritage5040184>

Academic Editor: Chiara Soffritti

Received: 29 September 2022

Accepted: 16 November 2022

Published: 18 November 2022

Publisher’s Note: MDPI stays neutral with regard to jurisdictional claims in published maps and institutional affiliations.



Copyright: © 2022 by the authors. Licensee MDPI, Basel, Switzerland. This article is an open access article distributed under the terms and conditions of the Creative Commons Attribution (CC BY) license (<https://creativecommons.org/licenses/by/4.0/>).

1. Introduction

Bronze disease is one of the major issues in bronze artwork conservation. It occurs as a cyclic phenomenon, which can lead to the pitting of the surface and the severe impairment of artifact properties until its destruction [1–6]. In the presence of chloride ions and high relative humidity [7], the copper may react, forming an inner layer of cuprous chloride (CuCl, nantokite), which is the first step toward bronze disease [1,8]. The active dissolution of nantokite causes the formation of porous cuprite (Cu₂O) and hydrochloric acid (HCl) [4,9]. Hydrochloric acid reacts with copper to form fresh nantokite, which, in turn, can generate cuprite and hydrochloric acid in a cyclic process [4,8,9]. The formation of an outer layer of green and powdery copper trihydroxychlorides (2Cu₂(OH)₃Cl, atacamite, and the polymorphs botallackite, clinoatacamite, and paratacamite) from the reaction of nantokite with water and oxygen, is the most evident consequence of the onset of bronze disease [1,9,10] (Figure 1). The conversion of nantokite to trihydroxychlorides, due to their larger volume, induces mechanical stress and the consequent cracking or fragmentation of the surface [11]. Therefore, the timely detection of even small amounts of corrosion products is crucial [3].

Techniques such as X-ray Diffraction (XRD), Confocal Micro-Raman (CMR) spectroscopy, X-ray Fluorescence (XRF) [3], and Scanning Electron Microscopy (SEM) have proven effective for the early detection of bronze disease [1–3,12–16]. Most of the former

bench-top techniques are invasive because they are based on micro-sampling, which is generally not representative of the overall distribution of corrosion products. Moreover, when dealing with huge outdoor monuments, portable or transportable techniques are desirable, allowing the analysis of the irregular and difficult-to-access surfaces also [1,2].

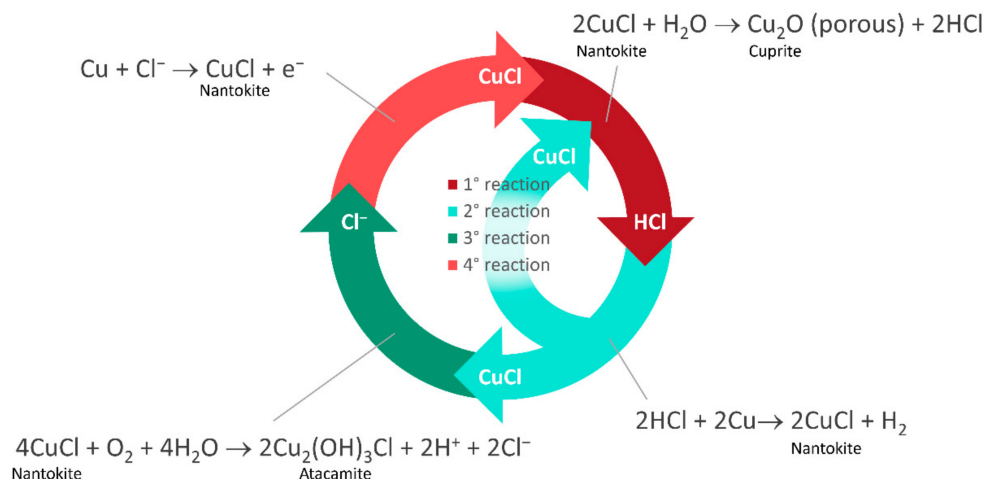


Figure 1. Schematic representation of the steps of the autocatalytic corrosive process.

Several instruments have been developed for the in-situ analysis of cultural heritage artifacts, among which handheld devices for Raman spectroscopy and X-ray fluorescence (p-XRF) enable rapid, non-invasive, and non-destructive analysis providing optimal results on most works of art (easel paintings, stone and metal artifacts, frescoes, and so on) [17–21].

For the characterization of bronze corrosion patinas, some authors [22,23] highlight how Raman spectroscopy can be a powerful approach to discriminate not only between atacamite and its polymorphs (which is crucial because the XRD patterns of $2\text{Cu}_2(\text{OH})_3\text{Cl}$ polymorphs are very similar [24]) but also between artificial and natural patinas [15,22,23].

In addition to the former analytical approaches, the use of less common techniques for the analysis of metal works of art, such as Fiber Optics Reflectance Spectroscopy (FORS) and Optical Coherence Tomography (OCT), is spreading. Based on selective absorption caused by molecular electronic transitions, the FORS technique is widely used on cultural heritage for the identification of materials, in particular for the characterization of pigments, dyes, and binders [18,25,26]. Liu [1] recently explored the potential of FORS in the spectral range of 1000–2500 nm to analyze corrosion products on bronze, exploiting the differences between atacamite and other common green corrosion products (i.e., nantokite, malachite, and chalconatronite).

OCT is a well-known technique in the study of varnishes and for monitoring the cleaning process [26–28] on easel paintings. Based on the Michelson interferometer [29], OCT devices allow for the acquisition of cross-sectional images of semi-transparent materials with micrometric resolution [27,28]. The application of OCT to metal artworks is quite new; recently, some authors applied OCT to study protective coatings on metals [30,31] and to distinguish corroded and uncorroded areas [30].

In this work, a comparison of several portable and bench-top instruments was carried out in order to identify a method for the early detection of corrosion based on non-invasive techniques. The performances of some commercial portable Raman devices (Bruker Optics BRAVO[®] and BWTEK BWS415 i-Raman) and a bench-top confocal device (Renishaw inVia[™]) were compared by performing measurements on artificially aged bronze samples.

FORS spectra in the range of 304–1709 nm were carried out on bronze samples where copper trihydroxychloride formation was induced for an in-depth characterization of the corrosion products.

Two OCT devices (with IR sources at 900 nm and 1300 nm, respectively) were used to obtain new information on the morphology of the surface stratigraphy of corrosion patinas.

Finally, OCT data from the bronze surfaces were compared with those obtained using SEM, which is traditionally employed to study the morphology of metals.

2. Materials and Methods

2.1. Materials

Two sets of bronze samples, purposely developed for a previous research project, were cast by Fonderia Salvatori, Florence, and supplied by Opificio delle Pietre Dure, Florence. The sets included 90–10 bronze (Cu 90 wt%, Sn 10 wt%) and silicon bronze (Cu 89 wt%, Si 9.9 wt%, Mn 0.9 wt%), representative of Florentine Renaissance workshops and modern works of art, respectively. The two different alloys were chosen to evaluate their impact on the morphology and composition of the corrosion products. These bronze specimens (Table 1) consisted of four individually cast squared coupons measuring $4.7 \times 4.7 \times 0.5$ cm (± 1 mm). Samples were polished using a Dremel rotary tool equipped with a drum mandrel (13 mm) fitting a sanding band sleeve (grid 240).

For the aging, hydrochloric acid (37%) by Carlo Erba, Italy, was used.

Table 1. Summary of the bronze samples studied in this work.

Sample Code	Bronze Alloy	Chemical Composition	Aging Conditions
A2 A3	Silicon Bronze	Cu 89 wt%, Si 9.9 wt%, Mn 0.9 wt%	HCl 0.5 M HCl 1 M
B2 B3	Bronze 90–10	Cu 90 wt%, Sn 10 wt%	HCl 0.5 M HCl 1 M

2.1.1. Artificial Aging

The bronze samples were exposed to acid vapors of aqueous HCl solutions (0.5 M and 1 M) inside sealed glass containers with a high humidity level ($\sim 100\%$ RH) (Figure 2). The glass containers were placed in an electrically heated stove ($50\text{ }^\circ\text{C}$) for 30 days.

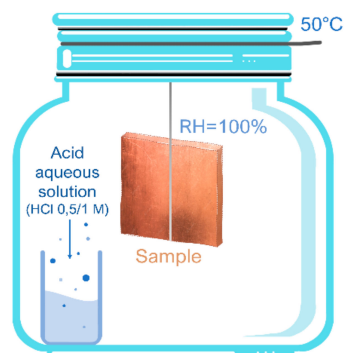


Figure 2. Schematization of the accelerated aging process. Samples were exposed to an acid atmosphere (HCl 0.5 M, HCl 1 M) in highly corrosive conditions (RH 100%, T $50\text{ }^\circ\text{C}$, time 30 days).

2.2. Methods

Confocal Raman Microspectroscopy was carried out on the surface of the artificially aged samples to assess the actual formation of copper trihydroxychlorides. The samples were then analyzed using a set of non-invasive methods for the in-situ analysis, based on the use of portable or transportable instruments, in order to evaluate their suitability for the early detection of bronze disease.

The Raman technique is well-established for the identification of corrosion products, and therefore two portable Raman devices were compared as regards the background noise, fluorescence, and sensitivity to clinoatacamite detection.

Conversely, the performance of the FORS technique, which is rarely used for this purpose but is very promising, was assessed.

For the high-resolution imaging of the surface, aimed both at studying its morphology and investigating the possibility of measuring the corrosion products' thickness, two SD-OCT devices were used. Finally, SEM analysis was carried out to cross-check the surface results obtained by OCT. The instruments used in this study are described in the following subsections.

2.2.1. Bench-top Confocal Raman Microspectroscopy (CRM)

The Raman micro-analyses were performed with a Renishaw inVia™ Raman confocal microscope, supplied with a Leica DM2700 optical microscope and a 532 nm excitation source, using a 50× long-distance objective (NA = 0.5; theoretical spot size: 0.65 μm). Spectra were acquired in the 100–3800 cm⁻¹ spectral range, with 1800 L/mm grating and a thermoelectrically cooled CCD detector (spectral range: 400–1060 nm, spectral resolution: 1 cm⁻¹/CCD pixel). A laser power of 0.5–2.5 mW and an integration time of 10 s with 1–5 accumulations were set. Data were processed using Wire5.1 and OriginPro 2022b software.

2.2.2. Handheld Raman Spectroscopy

Raman spectroscopy was performed with the handheld Bruker Optics BRAVO® spectrometer. The device allows fluorescence mitigation and background-free spectra collection thanks to patented sequentially shifted excitation (SSE™). The instrument has two excitation diode lasers (DuoLaser™, 785 and 852 nm) with a spot size of 0.1 × 0.5 mm². The lasers were detected by different areas of a CCD detector (spectral resolution 12 cm⁻¹). Data were acquired in two sequential spectral ranges: 170–2000 cm⁻¹ (laser at 852 nm) and 2000–3200 cm⁻¹ (laser at 785 nm). The two excitation lasers were temperature-shifted three times over a range of about 0.4 nm to obtain three spectrally shifted raw spectra (by 6 cm⁻¹) [21]. The output laser power—less than 100 mW—was set automatically. The detector integration time was 2000 ms, and 10 accumulations were acquired. Data were processed using OPUS-IR™ and OriginPro 2022b software.

2.2.3. Portable Raman

Raman spectra were also collected using the portable device BWTEK BWS415 i-Raman, equipped with a 532 nm excitation source (power 50 mW, spot size 85 μm) and a cooled linear array detector. An integration time of 6000 ms, with 2 multiplications and 4 repetitions, was set. Spectra were acquired in the spectral range of 400–4000 cm⁻¹, with a spectral resolution of 4 cm⁻¹. Data were processed using BWSpec and OriginPro 2022b software.

2.2.4. Fiber Optics Reflectance Spectroscopy (FORS)

Two Zeiss Multi-Channel Spectrometer (MCS) devices were used for FORS measurements: the MCS521 Vis-NIR extended module and the MCS511 NIR 1.7 module, operating in the spectral ranges of 304–1135 nm and 939–1709 nm, respectively. The spectra resolution was 3.2 nm in the visible (VIS) region and 6.0 nm in the near-infrared (NIR) region, and the spot size was about 3 mm.

Data were acquired with a 45°/0° illumination/detection geometry, and a 100% reflecting reference standard (Spectralon) was used for calibration. For each measurement point, three spectra were collected, which were the average of three spectra each. For each set of measurements, a different integration time was set to optimize the spectrum acquisition.

2.2.5. Spectral Domain Optical Coherence Tomography (SD-OCT)

Two commercial devices were used: Thorlabs Telesto-II and Ganymede Series Spectral-Domain OCT Systems equipped with both a superluminescent diode and a diffraction grating spectrograph with a fast camera. The Telesto-II operated at a central wavelength of 1300 nm with 170 nm bandwidth, 5.5 μm axial resolution of (in air), 13 μm lateral resolution, and maximum field of view (FOV) of 10.0 × 10.0 mm². The Ganymede worked at a central wavelength of 900 nm with 150 nm bandwidth; the axial resolution was 3 μm in air, and

the lateral resolution was 4 μm . The maximum field of view (FOV) was $6.0 \times 6.0 \text{ mm}^2$. The sample stage allowed the specimen to be moved along the XY axes and rotated, and the probe could be moved along the Z axis.

Data were acquired using the Telesto-II system with a FOV of $5 \times 5 \times 1 \text{ mm}$ and a voxel size of $6.5 \times 6.5 \times 3.55 \mu\text{m}$ and using the Ganymede system with a FOV of $3 \times 3 \times 0.4 \text{ mm}$ and voxel size of $3.55 \times 3.55 \times 1.96 \mu\text{m}$. Since the refractive index n of the patina could not be known a priori and is not tabulated, the acquisitions were performed considering $n = 1$. Data were processed with ThorImage 5.0 and ImageJ software.

2.2.6. Scanning Electron Microscopy (SEM)

An EVO[®]MA 25 Zeiss microscope was used for the surface imaging on the microscale. Samples with no preparations were observed under SEM at an accelerating voltage of 20 kV and beam current of 300 pA. Images were collected both in Back Scattered Electron (BSE) and Secondary Electron (SE) modes. ZEISS SmartSEM software was used to collect and process the data.

3. Results and Discussion

3.1. Characterization of the Artificial Patina

After 30 days under the highly corrosive conditions described in Section 2.1.1, all the samples showed a color change (Figure 3) due to the oxidation of the copper and the probable formation of a red-brown cuprite layer [8]. Under visual inspection, samples A2 and B3 exhibited a compact and uniform reddish patina; an extensive dark green patina had formed on the front surface of sample A3, while sample B2 showed limited pale green formations on the lower edge.

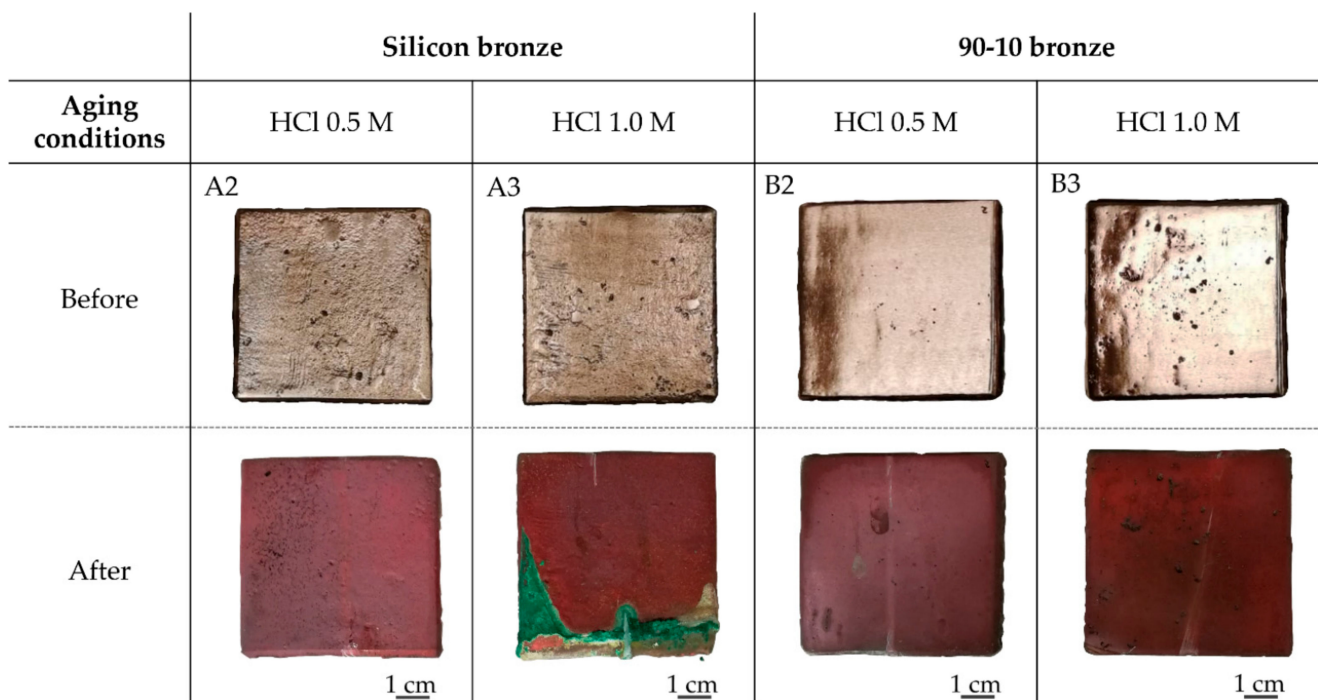


Figure 3. Photographs of samples before and after the accelerated aging process (RH 100%, T 50°C, time 30 days) in the presence of HCl 0.5 M (samples A2 and B2) and HCl 1.0 M (samples A3 and B3).

To characterize the patina's molecular composition and to confirm the formation of copper trihydroxychlorides, the surface of each sample was analyzed with a bench-top Confocal Raman Microspectroscopy (CRM). The optical microscopic examination (20 \times and 50 \times) revealed the presence of green crystals, even on samples seemingly covered only by the red layer (Figure 4).

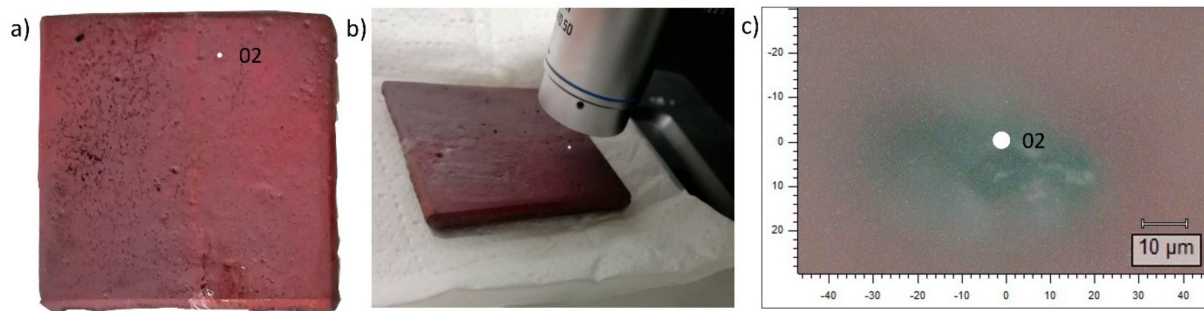


Figure 4. Sample A2: (a) macroscopic image; (b) point 02 during the CRM acquisition; (c) microscopic image (objective 50 \times) of a green crystal where the A2_02 spectrum was acquired (Figure 5).

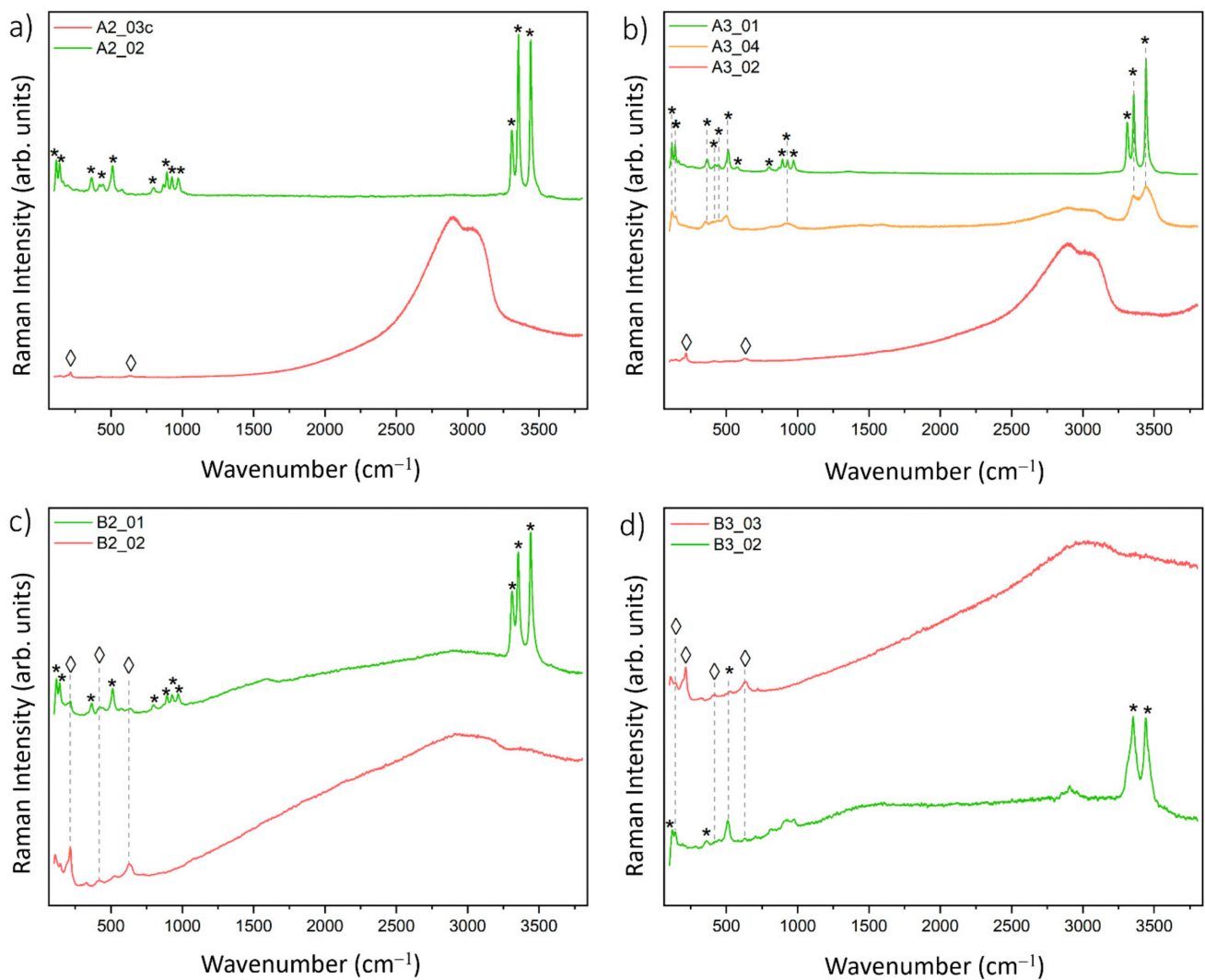


Figure 5. Raman spectra (obtained with 532 nm laser excitation) of (a) sample A2, measurement points 02 (green crystal) and 03 c (red layer); (b) sample A3, measurement points 01 (green patina), 02 (red layer) and 04 (green crystal); (c) sample B2, measurement points 01 (green crystal) and 02 (red layer); (d) sample B3, measurement points 02 (green crystal) and 03 (red layer). The peaks highlighted with the symbol * are attributed to copper trihydroxychlorides, while the symbol ◇ indicates the peaks ascribed to cuprite.

Raman spectra of the green crystals (A2_02, A3_04, B2_01, and B3_02 in Figure 5) and the green patina (A3_01 in Figure 5b) showed the characteristic features of copper hy-

droxychlorides: OH stretching vibrations were observed in the range 3300–3450 cm^{-1} [23]. Peaks in the spectral region of 800–1000 cm^{-1} are ascribed typically to OH- deformation modes [32], but some authors [23,25,33] assign them to Cu-O-H bending modes. The Raman signal in the range of 600–100 cm^{-1} is associated with O-Cu-O and Cl-Cu-Cl bending vibrations and lattice modes [23].

Comparing the acquired data with reference spectra found in the literature [23,32–34] (Table 2), bands at 892, 927, and 970 cm^{-1} were attributed to polymorph clinoatacamite [35].

Table 2. Raman spectra from artificially aged bronze samples (green corrosion products), compared with the reference clinoatacamite characteristic Raman lines found in the literature.

Artificial Patina (cm^{-1})				Clinoatacamite Ref. (cm^{-1}) [32–34]	Assignment
A2_02	A3_01	B2_01	B3_02		
				3475	
3445	3443	3444	3442	3443	-OH- stretching [23,34]
3356	3354	3353	3355	3357	
3311	3310	3313		3314	
966	970	970		969	-OH deformation [34]/ Cu-O-H bending [23,25]
929	930	928	972	927	
891	895	893	927	892	
	867			866	
800	801	799		799	
578	578	573		576	CuO stretching [34]
516	513	512	512	511	O-Cu-O asymmetric stretching [23]
452	445	447		445	Cu-Cl stretching [34]
417	419	419		420	
368	365	365	363	364	
				256	Cl-Cu-Cl bending [23,34]
				206	
				193	
				183	
				165	
142	140	142	142	142	
118	119	119	119	118	

Raman spectra collected on reddish-brown areas (Figure 5a, A2_03c; Figure 5b, A3_02; Figure 5c, B2_02; Figure 5d, B3_03) of each sample showed peaks at 143 cm^{-1} , 218 cm^{-1} , 414 cm^{-1} , and 630 cm^{-1} , which are attributed to Cu_2O [36–38]. The very low-intensity signal in the spectra in Figure 5a,b (red line) is due to the presence of artifacts (band at 2200–3200 cm^{-1}) [39], which were caused by the presence of unoriented cuprite crystals.

3.2. Instruments Comparison and Validation

3.2.1. Raman Spectroscopy

The handheld instrument, exploiting 852 nm excitation, did not provide useful data on samples A2, B2, and B3; the very high background hid the expected Raman peaks of cuprite and clinoatacamite. Despite the difficult interpretation due to the background noise, it was possible to recognize some characteristic peaks of atacamite in the spectra acquired from the green patina of sample A3 (Figure 6) at 364 cm^{-1} , 422 cm^{-1} , 512 cm^{-1} , 891 cm^{-1} , 921 cm^{-1} , and 963 cm^{-1} [34]. Usually, laser sources at 785 nm and 852 nm offer a good compromise between efficiency and low fluorescence [35], but in the case of green compounds, the red laser can produce spectra with very weak Raman peaks and high background noise because of the strong absorbance these pigments show at such wavelengths [35,40].

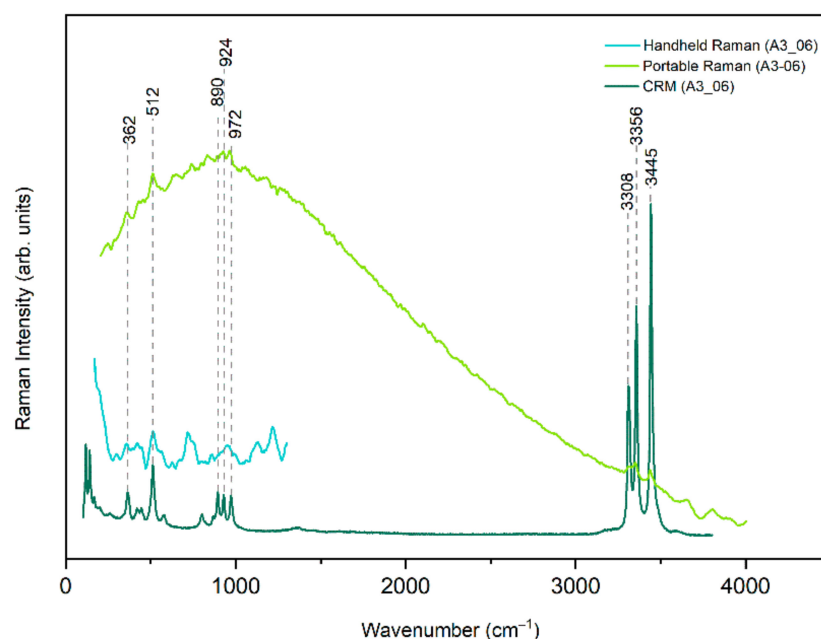


Figure 6. Raman spectra of the green patina on sample A3 (measurement point 06), obtained with the bench-top CRM (532 nm laser source), with the handheld Raman device (852 nm laser excitation) and with a portable device (532 nm laser source).

This problem is generally solved with long integration times, a lot of accumulations, and reduced laser power to avoid pigment damage [15,35,40], making the analysis very time-consuming. Therefore, instruments with green excitation lasers (532 nm) are usually preferred.

Spectra acquired using the portable Raman spectrometer, exploiting 532 nm excitation, were strongly affected by fluorescence that masks the Raman peaks. Especially on samples A2, B2, and B3, the fluorescence background overwhelmed the Raman signal because of the very low effective power of the instrument excitation source and the small amount of corrosion products on their surface. The spectra acquired from sample A3 showed weak but recognizable peaks that fit with the clinoatacamite spectrum: 366 cm^{-1} , 514 cm^{-1} , 926 cm^{-1} , 966 cm^{-1} , 3310 cm^{-1} , 3352 cm^{-1} , and 3441 cm^{-1} (Figure 6).

3.2.2. Fiber Optics Reflectance Spectroscopy

The surface of artificially aged bronze specimens was noninvasively characterized using the FORS technique, which enabled obtaining reflectance spectra by point measurements.

On samples A2, B2, and B3, FORS measurements were performed on three spots for each corrosion typology. Three areas were selected on sample A3 corresponding to the red-brown oxidation layer at the top, the darker green area on the left, and the lighter green area at the bottom. Three reflectance spectra were collected from each area. The average spectra for each sample are shown in Figure 7 (one spectrum for each area is shown for sample A3).

Samples A2, B2, B3, and the red area of A3 showed an absorption band at about 400–650 nm. They also exhibited a maximum at 463 nm except for sample B2. The green areas of A3 were characterized by a peak centered at 514 nm and two minima at 1467 nm and 1546 nm. The spectral features of samples A2, A3 (red area), B2, and B3 were compatible with cuprite, which is characterized by an absorption band between 400–650 nm [1] and inflection points at 490 nm, 595 nm, and 625–685 [41,42].

Data acquired from the green areas of A3 were in good agreement with the reflectance spectra found in the literature for copper trihydroxychlorides, which show a band centered at 510–530 nm and a narrow absorption at 1465 nm [1,43,44]. Liu [1] has assigned this

latter band to the first overtone of the OH stretching mode, although he specifies that the correct assignment of bands is questionable because spectroscopic studies in the near-infrared region on bronze corrosion products are not copious. In a recent paper, Liggins [43] highlighted the lack of reflectance spectra of atacamite and polymorphs. Moreover, a few papers report that the former composites have very similar spectra, especially in the range of 300–1000 nm [1,43]. For this reason, Liu and Liggins have focused their research in the range of 1000–2500 nm, where the possibility of discriminating copper trihydroxychlorides from other non-injurious green corrosion products is higher [1,43].

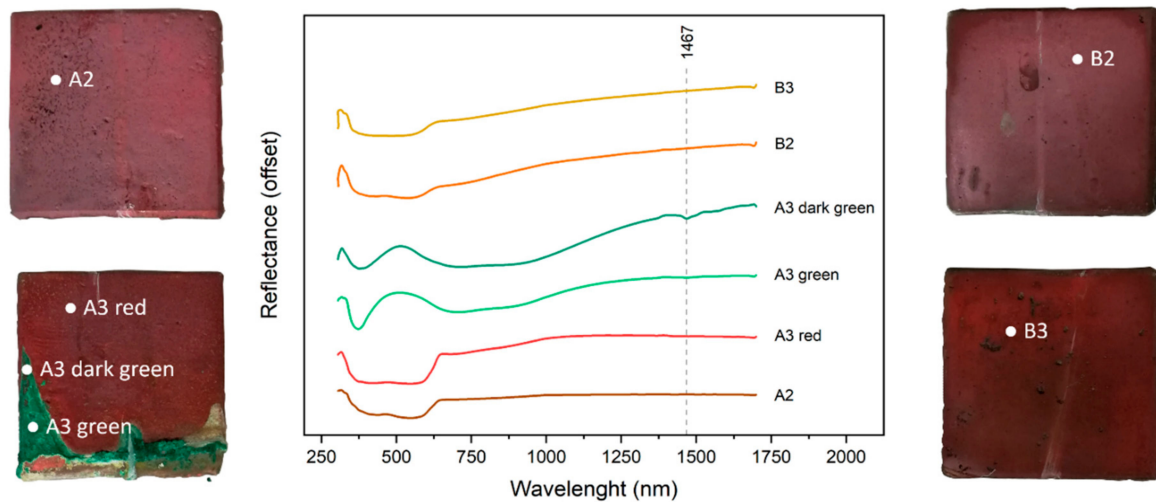


Figure 7. Average reflectance spectra calculated for each sample (A2, B2, B3) and three different areas of sample A3. Spectra were acquired in the range of 304–1709 nm.

3.2.3. Spectral Domain Optical Coherence Tomography

In order to study the micrometric morphology of the corroded surface and verify the possibility of measuring the features of the corrosion products, cross-sectional analyses were performed on the specimens. A $5 \times 5 \times 1$ mm tomocube (C-scan) was collected for each sample using the Telesto-II system (1300 nm central wavelength) and a $3 \times 3 \times 0.4$ mm tomocube using the Ganymede system (900 nm central wavelength). A Melinex mask was used to acquire the same areas with the two instruments. Figure 8 shows two C-scans acquired from sample A2 with the 900 nm (Figure 8a) and the 1300 nm (Figure 8c) device. The tomocubes in Figure 8a,c allowed for studying surface alteration and assessing whether the corrosive phenomenon resulted in the formation of micro-cracks or pitting. In Figure 8b,d, a B-scan (XZ-slice) acquired with the 900 nm and 1300 nm instruments is reported, showing the irregularity of the surface. The data demonstrated the utility of the OCT in surface monitoring and the measurability of the features.

The C-scans in Figure 9c,d were acquired from sample A3 in an area across the green patina of clinoatacamite and the cuprite oxidation layer (Figure 9a, and detail in Figure 9b). Figure 9c,d display the surface morphology of the corroded bronze. In Figure 9d, the rough appearance of the accumulation of corrosion products is particularly noticeable.

In the B-scans in Figure 9e,f, a double signal is present, pointing out the alteration layer, whose average thickness is $30 \pm 10 \mu\text{m}$ (this value must be divided by the refractive index). The slice acquired with the 1300 nm device (Figure 9f) shows some features that could be due to the partial detachment of the corrosion patina from the underlying pristine bronze.

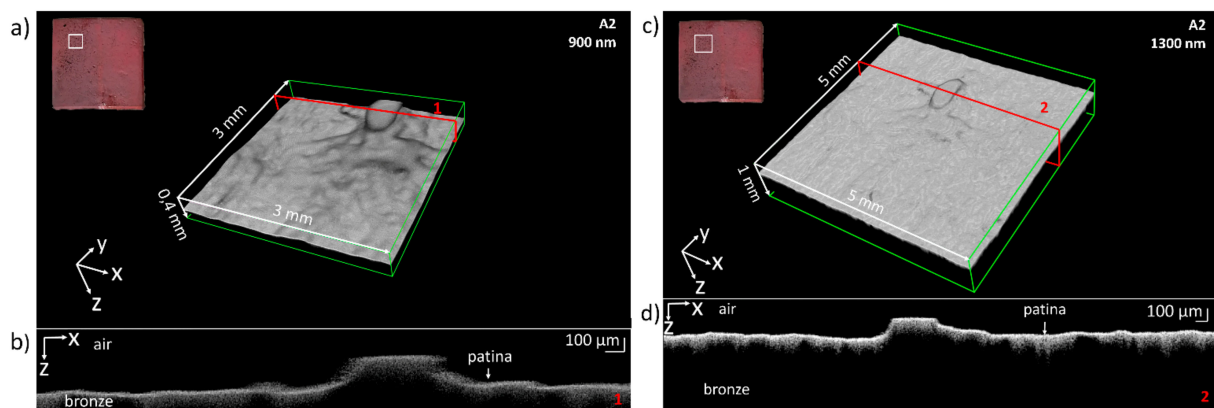


Figure 8. Sample A2: (a) In the left corner, the RGB image of the sample showing the measurement area (white box). In the center, the $3 \times 3 \times 0.4$ mm OCT tomocube acquired with the Ganymede system. (b) shows the position of the B-scan (in red); (c) on the corner, the RGB image of the sample with the location of the acquisition area (white box). In the center, the $5 \times 5 \times 1$ mm OCT tomocube acquired with the Telesto-II system. The red rectangle indicates the position of the XZ-slice shown in (d).

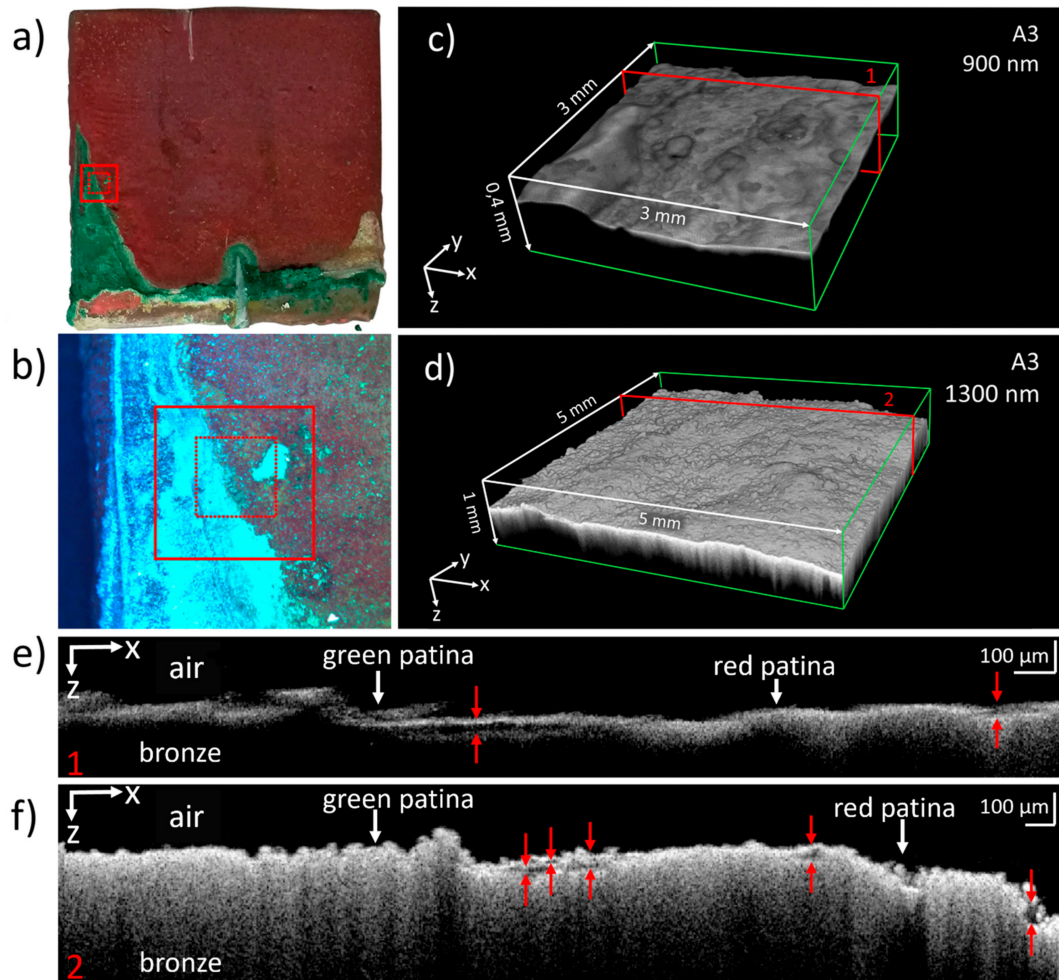


Figure 9. Sample A3: (a) RGB image, in red are shown the measurement areas of Telesto-II (solid line) and Ganymede (dashed); (b) detail of measurement area, obtained with the camera of Telesto-II; (c) $3 \times 3 \times 0.4$ mm OCT tomocube (acquired by the Ganymede system); (d) $5 \times 5 \times 1$ mm OCT tomocube (acquired with the Telesto-II system); (e) B-scan acquired using Ganymede along the XZ slice shown in red in (c); (f) B-scan acquired with Telesto-II along the XZ slice indicated by the red rectangle in (d).

3.2.4. Scanning Electron Microscopy

Due to the innovativeness of using the SD-OCT for the morphological analysis of the corrosion products on metals, Scanning Electron Microscopy, a well-established technique for the high-resolution imaging of surfaces, was also carried out to compare results.

SEM images were acquired both in backscattered electron mode (BSE) and secondary electron mode (SE). The cross-check between the results obtained with the two former techniques to ascertain the validity of the use of OCT was carried out using a Melinex mask to probe the same areas of the samples. For the morphological study, an area as large as possible was detected with the SEM (about 3 mm × 2 mm) within the area surveyed with OCT (5 mm × 5 mm) using the smaller magnification (60× objective). For the full exploitation of SEM potential, we would have used higher magnifications, but the measured area would not have been comparable with that analyzed by OCT. Figure 10 shows a detail of the surface of sample A2, where a small protuberance of about 1 mm × 0.5 mm, which is probably a casting defect, is clearly visible. Despite the different scale and resolution, this feature has been successfully detected with both the SD-OCT (Figure 10a) and the SEM (Figure 10b,c).

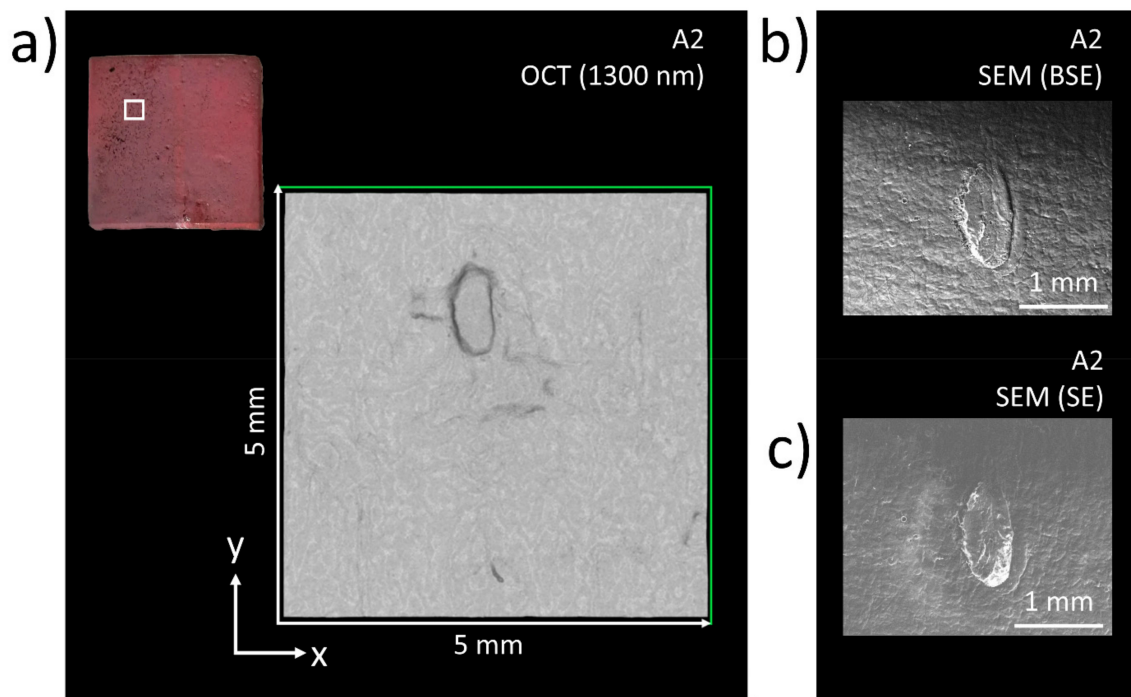


Figure 10. Sample A2: (a) left corner: the RGB image with the measurement area (highlighted in white). Center: 5 mm × 5 mm OCT image corresponding to the XY section of the tomocube acquired with the Telesto-II system; SEM image acquired (b) in backscattered electron mode and (c) in secondary electron mode.

4. Conclusions

The present study, aimed at the early detection of copper trihydroxychlorides on bronze artworks, was based on the comparison of the performances and characteristics of different portable/transportable instruments to define their areas of applicability and usefulness. The early detection of these compounds is crucial because their presence constitutes the main symptom of bronze disease.

The actual formation of copper trihydroxychlorides on samples was confirmed by Confocal Raman Microscopy (CRM) analysis.

Concerning portable Raman spectroscopy, the device operating at 532 nm proved to be more efficient as compared to the one at 852 nm, providing better signal-to-noise spectra characteristic of green bronze alterations. The results obtained with the two portable

instruments were consistent regarding the clinoatacamite found in the green patina of A3, albeit with different limitations due mainly to the high background noise. However, both portable instruments proved to be inefficient on samples A2, B2, and B3 because of either the used excitation laser wavelength or laser power issues, as well as the low concentrations of the analyte. The main limits of portable Raman devices regard the wavelength of the excitation source: the red lasers produce spectra with a low signal-to-noise ratio due to the strong absorbance that green pigments have at such wavelength. Therefore, the 532 nm source is best suited for the green compounds. Another limit is the high fluorescence that is due to the bronze alloy that can superimpose the Raman characteristics of little amounts of copper trihydroxychlorides.

The ability to detect basic copper chlorides by means of Fiber Optics Reflectance Spectroscopy (FORS) was verified in zones with high concentrations of analyte. Due to the versatility and easy-to-use characteristics of the instrument, FORS is an excellent solution for fast, on-site, non-invasive diagnostics. Its main limitation is the impossibility of distinguishing among the various polymorphs of atacamite. Nevertheless, FORS could have the potential for in-situ post-restoration monitoring. In fact, it could be useful for highlighting changes on the surface caused by the formation of green alteration compounds.

To the best of our knowledge, this is the first time that OCT has been used to characterize corrosion layers on artistic bronzes. The presented results, validated with SEM imaging performed at low resolution, demonstrated the effectiveness of the technique for measuring the features of corrosion products and analyzing surface morphology. Apart from the lower lateral resolution, OCT showed it possessed the following advantages compared to SEM: (i) no vacuum was needed, (ii) large and unmovable artworks could be studied in situ, (iii) no sampling or contact was required, and (iv) axial information. These latter characteristics made OCT well-suited for the study of incoherent and powdery corrosion layers that very often cannot be sampled due to their fragility.

Moreover, the acquired tomograms allowed the obtaining of stratigraphic information on the patina, generally based on micro-sampling. For the cross-sectional analysis of the corroded surface, the Telesto-II SD-OCT showed a better performance than Ganymede probably because the corrosion products were more transparent at 1300 nm than 900 nm (Telesto-II and Ganymede operating wavelength, respectively).

Therefore, the use of OCT for the study of artistic bronzes affected by bronze disease was shown to be very promising.

Under the applied aging conditions, neither morphological nor compositional differences were detected with the set of instruments used for the characterization of the patinas induced on the two alloys.

Author Contributions: Conceptualization, R.F. and D.P.; methodology, R.F., M.G., E.C., L.D., J.S. and D.P.; validation, D.P. and S.I.; formal analysis, D.P. and M.G.; investigation, D.P., M.G. and S.I.; resources, R.F. and E.C.; data curation, D.P.; writing—original draft preparation, D.P.; writing—review and editing, R.F., E.C., L.D., M.G., S.I. and J.S.; supervision, R.F. and E.C. All authors have read and agreed to the published version of the manuscript.

Funding: The BRAVO Bruker Sequentially Shifted Excitation Raman instrument was acquired through SHINE project funding (strengthening the Italian nodes of E-RIHS, Avviso 424/2018 dell’Azione II.1 PON R&I 2014–2020, DD n. 461 del 14-03-2019).

Institutional Review Board Statement: Not applicable.

Informed Consent Statement: Not applicable.

Data Availability Statement: The data presented in this study are available on reasonable request from the corresponding author.

Conflicts of Interest: The authors declare no conflict of interest.

References

1. Liu, W.; Li, M.; Wu, N.; Liu, S.; Chen, J. A new application of Fiber optics reflection spectroscopy (FORS): Identification of “bronze disease” induced corrosion products on ancient bronzes. *J. Cult. Herit.* **2021**, *49*, 19–27. [[CrossRef](#)]
2. Letardi, P. Testing New Coatings for Outdoor Bronze Monuments: A Methodological Overview. *Coatings* **2021**, *11*, 131. [[CrossRef](#)]
3. Garmay, A.V.; Oskolok, K.V.; Monogarova, O.V. μ XRF Analysis of XVIII Century Copper Coin: Patina Investigation and “Bronze Disease” Detection. *Mosc. Univ. Chem. Bull.* **2021**, *76*, 133–136. [[CrossRef](#)]
4. MacLeod, I.D. Bronze Disease: An Electrochemical Explanation. *ICCM Bull.* **1981**, *7*, 16–26. [[CrossRef](#)]
5. Scott, D.A. A Review of Copper Chlorides and Related Salts in Bronze Corrosion and as Painting Pigments. *Stud. Conserv.* **2000**, *45*, 39–53. [[CrossRef](#)]
6. Casaletto, M.P.; De Caro, T.; Ingo, G.M.; Riccucci, C. Production of reference “ancient” Cu-based alloys and their accelerated degradation methods. *Appl. Phys. A* **2006**, *83*, 617–622. [[CrossRef](#)]
7. Papadopoulou, O.; Delagrammatikas, M.; Vassiliou, P.; Grassini, S.; Angelini, E.; Gouda, V. Surface and interface investigation of electrochemically induced corrosion on a quaternary bronze. *Surf. Interface Anal.* **2014**, *46*, 771–775. [[CrossRef](#)]
8. Grayburn, R.; Dowsett, M.; Hand, M.; Sabbe, P.-J.; Thompson, P.; Adriaens, A. Tracking the progression of bronze disease—A synchrotron X-ray diffraction study of nantokite hydrolysis. *Corros. Sci.* **2015**, *91*, 220–223. [[CrossRef](#)]
9. Bozzini, B.; Alemán, B.; Amati, M.; Boniardi, M.; Caramia, V.; Giovannelli, G.; Gregoratti, L.; Kazemian Abyaneh, M. Novel insight into bronze disease gained by synchrotron-based photoelectron spectro-microscopy, in support of electrochemical treatment strategies. *Stud. Conserv.* **2017**, *62*, 465–473. [[CrossRef](#)]
10. Di Francia, E.; Lahoz, R.; Neff, D.; de Caro, T.; Angelini, E.; Grassini, S. Laser-cleaning effects induced on different types of bronze archaeological corrosion products: Chemical-physical surface characterisation. *Appl. Surf. Sci.* **2022**, *573*, 150884. [[CrossRef](#)]
11. Scott, D.A. *Copper and Bronze in Art: Corrosion, Colorants, Conservation*; Getty Publications: Los Angeles, CA, USA, 2002; ISBN 978-0-89236-638-5.
12. Cosano, D.; Esquivel, D.; Mateos, L.D.; Quesada, F.; Jiménez-Sanchidrián, C.; Ruiz, J.R. Spectroscopic analysis of corrosion products in a bronze cauldron from the Late Iberian Iron Age. *Spectrochim. Acta. A. Mol. Biomol. Spectrosc.* **2018**, *205*, 489–496. [[CrossRef](#)]
13. Chang, T.; Maltseva, A.; Volovitch, P.; Odnevall Wallinder, I.; Leygraf, C. A mechanistic study of stratified patina evolution on Sn-bronze in chloride-rich atmospheres. *Corros. Sci.* **2020**, *166*, 108477. [[CrossRef](#)]
14. Ingo, G.M.; Riccucci, C.; Giuliani, C.; Faustoferri, A.; Pierigè, I.; Fierro, G.; Pascucci, M.; Albini, M.; Di Carlo, G. Surface studies of patinas and metallurgical features of uncommon high-tin bronze artefacts from the Italic necropolises of ancient Abruzzo (Central Italy). *Appl. Surf. Sci.* **2019**, *470*, 74–83. [[CrossRef](#)]
15. Coccato, A.; Bersani, D.; Coudray, A.; Sanyova, J.; Moens, L.; Vandenabeele, P. Raman spectroscopy of green minerals and reaction products with an application in Cultural Heritage research. *J. Raman Spectrosc.* **2016**, *47*, 1429–1443. [[CrossRef](#)]
16. Robotti, S.; Rizzi, P.; Soffritti, C.; Garagnani, G.L.; Greco, C.; Facchetti, F.; Borla, M.; Operti, L.; Agostino, A. Reliability of portable X-ray Fluorescence for the chemical characterisation of ancient corroded copper-tin alloys. *Spectrochim. Acta Part B At. Spectrosc.* **2018**, *146*, 41–49. [[CrossRef](#)]
17. Li, Y.; Wang, F.; Ma, J.; He, K.; Zhang, M. Study on the pigments of Chinese architectural colored drawings in the Altar of Agriculture (Beijing, China) by portable Raman spectroscopy and ED-XRF spectrometers. *Vib. Spectrosc.* **2021**, *116*, 103291. [[CrossRef](#)]
18. Gargano, M.; Galli, A.; Bonizzoni, L.; Alberti, R.; Aresi, N.; Caccia, M.; Castiglioni, I.; Interlenghi, M.; Salvatore, C.; Ludwig, N.; et al. The Giotto’s workshop in the XXI century: Looking inside the “God the Father with Angels” gable. *J. Cult. Herit.* **2019**, *36*, 255–263. [[CrossRef](#)]
19. Ruberto, C.; Mazzinghi, A.; Massi, M.; Castelli, L.; Czelusniak, C.; Palla, L.; Gelli, N.; Betuzzi, M.; Impallaria, A.; Brancaccio, R.; et al. Imaging study of Raffaello’s “La Muta” by a portable XRF spectrometer. *Microchem. J.* **2016**, *126*, 63–69. [[CrossRef](#)]
20. Dal Fovo, A.; Striova, J.; Pampaloni, E.; Fedele, A.; Morita, M.M.; Amaya, D.; Grazi, F.; Cimò, M.; Cirrincione, C.; Fontana, R. Rubens’ painting as inspiration of a later tapestry: Non-invasive analyses provide insight into artworks’ history. *Microchem. J.* **2020**, *153*, 104472. [[CrossRef](#)]
21. Innocenti, S.; Quintero Balbas, D.; Pezzati, L.; Fontana, R.; Striova, J. Portable Sequentially Shifted Excitation Raman Spectroscopy to Examine Historic Powders Enclosed in Glass Vials. *Sensors* **2022**, *22*, 3560. [[CrossRef](#)]
22. Privitera, A.; Corbascio, A.; Calcani, G.; Della Ventura, G.; Ricci, M.A.; Sodo, A. Raman approach to the forensic study of bronze patinas. *J. Archaeol. Sci. Rep.* **2021**, *39*, 103115. [[CrossRef](#)]
23. Bertolotti, G.; Bersani, D.; Lottici, P.P.; Alesiani, M.; Malcherek, T.; Schlüter, J. Micro-Raman study of copper hydroxychlorides and other corrosion products of bronze samples mimicking archaeological coins. *Anal. Bioanal. Chem.* **2012**, *402*, 1451–1457. [[CrossRef](#)] [[PubMed](#)]
24. Di Carlo, G.; Giuliani, C.; Riccucci, C.; Pascucci, M.; Messina, E.; Fierro, G.; Lavorgna, M.; Ingo, G.M. Artificial patina formation onto copper-based alloys: Chloride and sulphate induced corrosion processes. *Appl. Surf. Sci.* **2017**, *421*, 120–127. [[CrossRef](#)]
25. Liu, X.D.; Meng, D.D.; Zheng, X.G.; Hagihala, M.; Guo, Q.X. Mid-IR and Raman Spectral Properties of Clinoatacamite-Structure Basic Copper Chlorides. *Adv. Mater. Res.* **2011**, *146*, 1202–1205. [[CrossRef](#)]

26. Dal Fovo, A.; Oujja, M.; Sanz, M.; Martínez-Hernández, A.; Cañamares, M.V.; Castillejo, M.; Fontana, R. Multianalytical non-invasive characterization of phthalocyanine acrylic paints through spectroscopic and non-linear optical techniques. *Spectrochim. Acta. A. Mol. Biomol. Spectrosc.* **2019**, *208*, 262–270. [[CrossRef](#)] [[PubMed](#)]
27. Dal Fovo, A.; Tservelakis, G.J.; Klironomou, E.; Zacharakis, G.; Fontana, R. First combined application of photoacoustic and optical techniques to the study of an historical oil painting. *Eur. Phys. J. Plus* **2021**, *136*, 757. [[CrossRef](#)]
28. Iwanicka, M.; Moretti, P.; van Oudheusden, S.; Sylwestrzak, M.; Cartechini, L.; van den Berg, K.J.; Targowski, P.; Miliani, C. Complementary use of Optical Coherence Tomography (OCT) and Reflection FTIR spectroscopy for in-situ non-invasive monitoring of varnish removal from easel paintings. *Microchem. J.* **2018**, *138*, 7–18. [[CrossRef](#)]
29. Targowski, P.; Iwanicka, M. Optical Coherence Tomography: Its role in the non-invasive structural examination and conservation of cultural heritage objects—A review. *Appl. Phys. A* **2012**, *106*, 265–277. [[CrossRef](#)]
30. Lenz, M.; Mazzon, C.; Dillmann, C.; Gerhardt, N.C.; Welp, H.; Prange, M.; Hofmann, M.R. Spectral Domain Optical Coherence Tomography for Non-Destructive Testing of Protection Coatings on Metal Substrates. *Appl. Sci.* **2017**, *7*, 364. [[CrossRef](#)]
31. Quintero Balbas, D.; Dal Fovo, A.; Porcu, D.; Chaban, A.; Porcinai, S.; Fontana, R.; Striova, J. Non-Invasive Evaluation of Polymeric Protective Coatings for Metal Surfaces of Cultural Heritage Objects: Comparison of Optical and Electromagnetic Methods. *Appl. Sci.* **2022**, *12*, 7532. [[CrossRef](#)]
32. Frost, R.L.; Martens, W.; Kloprogge, J.T.; Williams, P.A. Raman spectroscopy of the basic copper chloride minerals atacamite and paratacamite: Implications for the study of copper, brass and bronze objects of archaeological significance. *J. Raman Spectrosc.* **2002**, *33*, 801–806. [[CrossRef](#)]
33. Ropret, P.; Kosec, T. Raman investigation of artificial patinas on recent bronze—Part I: Climatic chamber exposure. *J. Raman Spectrosc.* **2012**, *43*, 1578–1586. [[CrossRef](#)]
34. Frost, R.L. Raman spectroscopy of selected copper minerals of significance in corrosion. *Spectrochim. Acta. A. Mol. Biomol. Spectrosc.* **2003**, *59*, 1195–1204. [[CrossRef](#)]
35. Vandenaabeele, P.; Lambert, K.; Matthys, S.; Schudel, W.; Bergmans, A.; Moens, L. In situ analysis of mediaeval wall paintings: A challenge for mobile Raman spectroscopy. *Anal. Bioanal. Chem.* **2005**, *383*, 707–712. [[CrossRef](#)]
36. Montoya, N.; Montagna, E.; Lee, Y.; Doménech-Carbó, M.T.; Doménech-Carbó, A. Raman spectroscopy characterization of 10-cash productions from the late Chinese emperors to the Republic. *J. Raman Spectrosc.* **2017**, *48*, 1337–1345. [[CrossRef](#)]
37. Cho, N.C.; Jang, M.K.; Huh, I.K. A Study on the Microstructure and Corrosion Characteristics of Early Iron Age Bronze Mirrors Excavated from the Korean Peninsula. *Appl. Sci.* **2021**, *11*, 2441. [[CrossRef](#)]
38. Colomban, P.; Tournié, A.; Maucuer, M.; Meynard, P. On-site Raman and XRF analysis of Japanese/Chinese bronze/brass—the search for specific Raman signatures. *J. Raman Spectrosc.* **2012**, *43*, 799–808. [[CrossRef](#)]
39. Cuprite R140763. RRUFF Database: Raman, X-ray, Infrared, and Chemistry. Available online: <https://rruff.info/cuprite/R140763> (accessed on 30 August 2022).
40. Dominguez-Vidal, A.; de la Torre-López, M.J.; Campos-Suñol, M.J.; Rubio-Domene, R.; Ayora-Cañada, M.J. Decorated plasterwork in the Alhambra investigated by Raman spectroscopy: Comparative field and laboratory study. *J. Raman Spectrosc.* **2014**, *45*, 1006–1012. [[CrossRef](#)]
41. Bandiera, M.; Verità, M.; Lehuédé, P.; Vilarigues, M. The Technology of Copper-Based Red Glass Sectilia from the 2nd Century AD Lucius Verus Villa in Rome. *Minerals* **2020**, *10*, 875. [[CrossRef](#)]
42. Bersani, D.; Saviane, L.; Morigi, A.; Mantovani, L.; Aceto, M.; Fornasini, L. Multi-technique characterization of glass mosaic tesserae from Villa di Teodorico in Galeata (Italy). *J. Raman Spectrosc.* **2021**, *52*, 2234–2245. [[CrossRef](#)]
43. Liggins, F.; Vichi, A.; Liu, W.; Hogg, A.; Kogou, S.; Chen, J.; Liang, H. Hyperspectral imaging solutions for the non-invasive detection and automated mapping of copper trihydroxychlorides in ancient bronze. *Herit. Sci.* **2022**, *10*, 142. [[CrossRef](#)]
44. De Ferri, L.; Mazzini, F.; Vallotto, D.; Pojana, G. In situ non-invasive characterization of pigments and alteration products on the masonry altar of S. Maria ad Undas (Idro, Italy). *Archaeol. Anthropol. Sci.* **2019**, *11*, 609–625. [[CrossRef](#)]